Assessment of the Main Wind Force Resisting System Provisions of ASCE/SEI 7-22 for Rigid Buildings

Gregory A. Kopp, M.ASCE[1]; Jin Wang, M.ASCE[2]; Yitian Guo[3]; Stefano Brusco[4]; and Timothy John Acosta[5]

Abstract: In the provisions of ASCE/SEI 7-22, there are two philosophically different methods provided for the main wind force resisting system (MWFRS) loads in Chapter 27 and 28. The objective of this paper is to compare these two chapters with the up-to-date experimental observations, and to examine in detail how the differences arise for rigid buildings (i.e., neglecting flexibility/resonance effects). The study focuses on two major aspects: (1) examining differences due to utilizing the nondimensional building geometry ratios, and (2) examining the differences due to the theoretical gust effects models in Chapter 27. Wind tunnel data for 50 building shapes are employed. It is observed that the use of nondimensional building shape parameters allows for more accurate modeling of the wind loads. This has some effects on Chapter 27 loads but is particularly important for Chapter 28 where the effects of differing building shapes are not accounted for. For Chapter 27, although the mean coefficients are mostly reasonable, some of the peak loads are significantly different in magnitude when compared with the experimental data, being mostly underestimated. This is primarily due to the fact that the theoretically-calculated gust effects do not capture the actual measured turbulence effects. **DOI: 10.1061/JSENDH.STENG-14984.**

Introduction

In the provisions of ASCE/SEI 7-22, there are two methods provided for the main wind force resisting system (MWFRS) loads, which are based on different philosophical approaches. The most significant difference is that the procedure of Chapter 27 uses mean load coefficients and determines the peak aerodynamic loads using a theoretical model for the gust effects. This method, called the directional method, can be applied to buildings of all heights (i.e., all heights below the maximum height limit). This approach enables the inclusion of both the background (buffeting) response to wind gusts as well as the resonant response to capture building flexibility effects. It was originally developed for high-rise buildings for which the resonant response governs (Davenport 1967; Solari 1993a, b; Solari and Kareem 1998). In contrast, Chapter 28, called the envelope method, utilizes directly measured peak load effects considering structural influence functions. It is only applicable for rigid low-rise structures. Low-rise buildings have not typically been considered to have resonant responses, and the higher levels of turbulence and the non-Gaussian features of the wind loading means that only the peak pressures are typically required for design. However, it is important to note that these still represent equivalent static wind loads (ESWL) even though any possible resonant effects are neglected.

Further to this, there is a significant difference in the approach to the pressure coefficients. In Chapter 27, the pressure coefficients are fixed for windward ($Cp = +0.8$) and side ($Cp = -0.7$) walls. However, leeward walls depend on the length, L, to breadth, B, ratios, where L and B depend on the wind direction as shown in Fig. 1, and roofs depend on the height, h, to L ratios as well as the roof shape (see Fig. 27.3-1 in ASCE/SEI 7-22). In contrast, in Chapter 28 the pressure coefficients only depend on roof slope, although it is noted that the roof slope does alter the windward wall pressure coefficients. However, for a fixed roof slope, the pressure coefficients are unchanging with building shape.

Thus, it is unsurprising that the wind loads in the two chapters differ. The objective of this paper is to examine in detail how the differences arise for the background (nonresonant) load effects and compare these to experimental observations using a database of about 50 building shapes. In particular, the study will focus on two major aspects: (1) examining differences due to building shape via nondimensional geometry ratios, and (2) examining the differences due to the theoretical gust effect model used in Chapter 27. Only the background response is considered herein; flexibility effects and the gust effect factor model as applied to low-rise buildings will be the subject of a future study.

Theoretical Gust Effects for Rigid Buildings

The provisions of ASCE 7-22 directional method are based on the use of mean wind load coefficients combined with a gust effect factor, G. This approach allows the straight-forward combination of the background response, also called buffeting, with the resonant response for flexible buildings, as discussed in the introduction. The method originally emerged in the 1960s from the work of

[1]Professor, Faculty of Engineering, Western Univ., London, ON, Canada N6A 5B9 (corresponding author). ORCID: https://orcid.org/0000-0002-0784-3014. Email: gakopp@uwo.ca

[2]Assistant Professor, Faculty of Engineering, Western Univ., London, ON, Canada N6A 5B9. Email: jwan2225@uwo.ca

[3]Postdoctoral Associate, Faculty of Engineering, Western Univ., London, ON, Canada N6A 5B9. ORCID: https://orcid.org/0000-0003-2832-6507. Email: yguo287@uwo.ca

[4]Postdoctoral Associate, Faculty of Engineering, Western Univ., London, ON, Canada N6A 5B9. ORCID: https://orcid.org/0000-0003-0472-9133. Email: sbrusco@uwo.ca

[5]Doctoral Candidate, Faculty of Engineering, Western Univ., London, ON, Canada N6A 5B9. ORCID: https://orcid.org/0000-0002-5454-6063. Email: tacosta@uwo.ca

Note. This manuscript was submitted on January 22, 2025; approved on July 11, 2025; published online on September 29, 2025. Discussion period open until February 28, 2026; separate discussions must be submitted for individual papers. This paper is part of the ***Journal of Structural Engineering***, © ASCE, ISSN 0733-9445.

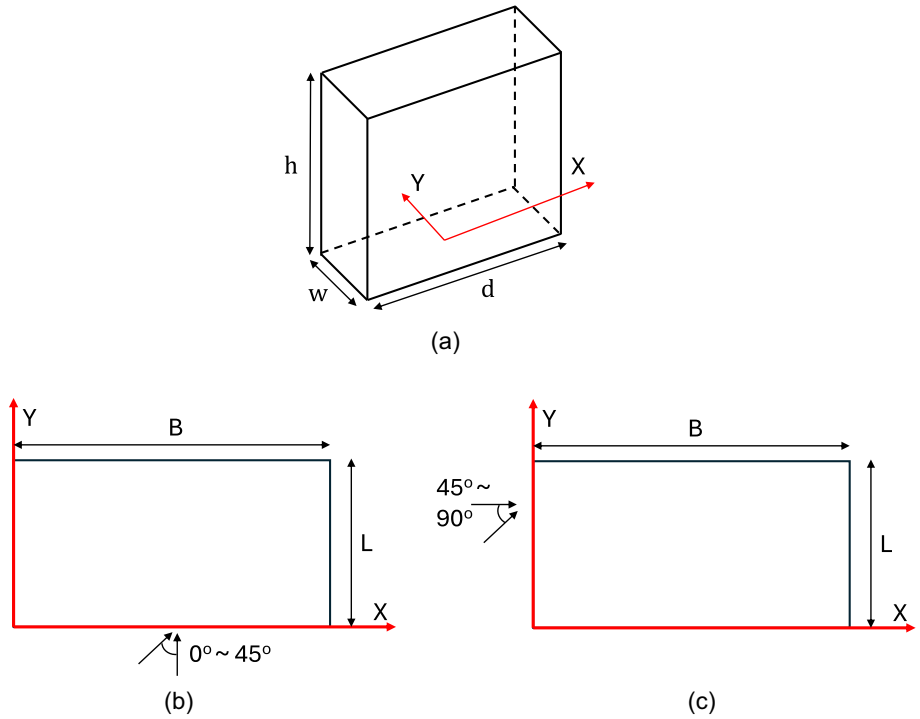

Fig. 1. Definition sketch of (a) building geometric parameters; and (b and c) building breadth, B, and length, L, as function of wind direction.

Davenport (1967). The measurement technology of the time allowed for the measurement of mean force coefficients using base balances, with the peak loads caused by wind gusts calculated from theory. Much of the data for the mean pressure/load coefficients in ASCE 7 came from Akins et al. (1977). Table 1 provides the geometries of their models.

For ASCE 7-98 the theoretical model was updated, using the gust effect factor model developed by Solari (1993a, b) and Solari and Kareem (1998). The theory is reviewed as follows, focusing only on the rigid buildings.

The peak pressure can be written as

$$\hat{P} = \overline{P} + g_P \sigma_P \tag{1}$$

where the ^ = peak value, the overbar a mean value; P = pressure; g = peak factor; σ = standard deviation; and the subscript P also signifies pressure. Without derivation, the gust effect factor, G, for a rigid building is

$$G = \frac{\hat{P}}{\hat{q}_z \overline{Cp}} = \frac{G_P}{G_u^2} = \frac{1 + g_P \frac{\sigma_P}{\overline{P}}}{G_u^2} = \frac{1 + 2 g_P I_u Q}{(1 + g_u I_u)^2} \tag{2}$$

where G_P = gust response factor; G_u = gust factor for the velocity; I_u = turbulence intensity, the subscript u represents the wind speed in the direction of the wind; q_z = dynamic wind pressure at height, z; and Q = background response factor

$$Q = \frac{\sigma_P}{\overline{P}} \frac{1}{2 I_u} = \frac{1}{2} \frac{\sigma_P}{\overline{P}} \frac{\overline{u}}{\sigma_u} \tag{3}$$

The background response factor Q = ratio of the pressure (or load) coefficient of variation (CoV) to the wind speed (i.e., turbulence intensity).

Here, the focus is on $G_P = 1 + 2 g_P I_u Q$, since the method to calculate G_u is well established (Holmes et al. 2014). Of importance are the two parameters: the peak factor, g_P, and the background response factor, Q. Solari (1993a, b) and Solari and Kareem (1998)

Table 1. The Akins et al. (1977) wind tunnel building geometries

Building index	Width, w (m, model scale)	Depth, d (m, model scale)	Roof height, h (m, model scale)	w/d	h/w
A	0.127	0.127	0.254	1.00	2
B	0.127	0.127	0.508	1.00	4
C	0.254	0.254	0.254	1.00	1
D	0.032	0.064	0.254	0.50	8
E	0.064	0.127	0.254	0.50	4
F	0.127	0.254	0.254	0.50	2
G	0.127	0.254	0.508	0.50	4
H	0.254	0.508	0.254	0.50	1
J	0.032	0.127	0.254	0.25	8
K	0.064	0.254	0.254	0.25	4
L	0.127	0.508	0.254	0.25	2
M	0.127	0.508	0.508	0.25	4
N	0.254	1.016	0.254	0.25	1

developed the theoretical solutions for G_P. The primary assumptions in the theoretical development are that:

- Quasi-steady theory (QST) can be used to estimate the gust effects such that the pressure (or load) fluctuations, P', are linearly proportional to the velocity fluctuations, u'. The aerodynamic admittance function is introduced to convert the velocity to a load, accounting for the effects of small-scale turbulence, which are assumed to be uncorrelated over the size of the body.
- Averaging time effects are relevant for the structural loading to account for gust effects, which are accounted for by filtering the wind velocity. The existing provisions had applied a 3-s filter to account for 3-s gust durations (Solari and Kareem 1998).
- All of the stochastic variations are assumed to have Gaussian distributions.

Then, based on QST, the instantaneous pressure can be expressed as

$$P = \frac{1}{2}\rho(\overline{u} + u')^2 \overline{C}p \tag{4}$$

where u' = fluctuating wind speed (neglecting the lateral and vertical fluctuations). Eq. (4) can be rewritten as

$$P = \frac{1}{2}\rho(\overline{u}^2 + 2\overline{u}u' + u'^2)\overline{C}p \approx \frac{1}{2}\rho(\overline{u}^2 + 2\overline{u}u')\overline{C}p \tag{5}$$

where the square of the fluctuating wind speed u'^2 is commonly neglected, assuming the turbulence intensity is small. Hence, the fluctuating pressure is described by

$$P' = \rho\overline{u}u'\overline{C}p = 2\frac{u'}{\overline{u}}\left(\frac{1}{2}\rho\overline{u}^2\overline{C}p\right) = 2\frac{u'}{\overline{u}}\overline{P} \tag{6}$$

where P' = fluctuating pressure. Solari (1993a, b) developed the gust effect factor model from the perspective of the frequency domain. Writing Eq. (6) in terms of the power spectral density yields

$$\int_0^\infty S_P(f)\cdot df = 4\frac{\overline{P}^2}{\overline{u}^2}\int_0^\infty S_u(f)\cdot df \tag{7}$$

where $S_P(f)$ and $S_u(f)$ are the pressure and wind speed spectra, respectively. Hence,

$$S_P(f) = 4\frac{\overline{P}^2}{\overline{u}^2}S_u(f) \tag{8}$$

For large structures, the velocity fluctuations do not occur simultaneously over all of the building surfaces and their correlation over the whole area, A, must be considered. The aerodynamic admittance function, $\chi^2(f)$, is introduced to allow for this effect. It is noted that when pressure coefficient time histories are available and integrated spatially over the building surfaces, the aerodynamic admittance function arises naturally without need for filtering.

The Solari and Kareem (1998) model for the gust effect factor includes a temporal filter function,

$$X(f,\tau) = \frac{\sin^2(\pi f\tau)}{(\pi f\tau)^2} \tag{9}$$

where τ is the averaging time. Therefore, the pressure spectra can be obtained by

$$S_P(f) = 4\frac{\overline{P}^2}{\overline{u}^2}S_u(f)\chi^2(f)X(f,\tau) \tag{10}$$

Thus,

$$G_P = 1 + g_P\frac{\sigma_P}{\overline{P}} = 1 + 2g_P I_u\sqrt{\int_0^\infty \frac{S_u(f)}{\sigma_u^2}\chi^2(f)X(f,\tau)df} \tag{11}$$

It should be noted that the filter in Eq. (11) is for the pressure loading, which is done separately from the filtering of the velocity that is used to obtain G_u. Comparisons of the wind tunnel data with the model in ASCE 7, both with and without the filter, are made as follows, noting that the envelope method of Chapter 28 has no explicit temporal filtering of the load. (The filters used with the current data analysis are discussed further in the section "Data Analysis" and in Guo et al. 2025.)

Solari and Kareem (1998) adopted an aerodynamic admittance function for overall loads as,

$$\chi^2(f) = \varsigma\left\{0.4\frac{fC_xB}{\overline{u}(h)}\right\}\varsigma\left\{0.4\frac{fC_zH}{\overline{u}(h)}\right\} \tag{12}$$

$$\varsigma\{\eta\} = \frac{1}{\eta} - \frac{1}{2\eta^2}(1 - e^{-2\eta}) \tag{13}$$

where C_x and C_z = lateral and vertical exponential decay coefficients in the coherence function, which are assumed to be 11.5 in their model; and $\overline{u}(h)$ = mean wind speed at the mean roof height, h. The constants C_x and C_z were derived from the coherence of wind speed measurements where the coherence of pressures is assumed to be proportional to the coherence of the fluctuating wind speed.

Since ASCE 7-02, the value of the gust effect factor, $G = 0.85$ has been permitted without calculation for rigid buildings in all terrains, although an adjustment factor of 0.925 was used to match this to existing loads of the time. In other words, the value of $G = 0.85$ was obtained by reducing the value from the theoretical calculation.

Methodology

Data Sources

Two sets of wind tunnel data are used herein. The first set is for rectangular plan building models with flat roofs for mid and high-rise structures from Wang and Kopp (2020a, b). The data set contains 24 building models with plan ratios, d/w, varying from 1 to 4, and height ratios, h/w, varying from 1 to 8, as shown in Table 2 with d and w being the depth and width (least horizontal dimension), respectively, as shown in Fig. 1. The second set is the Western University's contribution to the National Institute of Standard and Technology (NIST) database for low-rise structures as described in Ho et al. (2005). In total, 26 building models with low-sloped roofs are employed for the current study, with details shown in Table 3. Details of the wind tunnel tests for both studies can be found in Ho et al. (2005) and Wang and Kopp (2020a, b) and are not repeated here for brevity.

Data Analysis

Selected peak ESWL coefficients [which we will refer to as aerodynamic coefficients, $[GCp]$ or $(G)(Cp)$, following the Chapter 28 nomenclature since we are only considering the response caused by nonresonant gust effects] are calculated from the experimental data and compared to the results provided in Chapters 27 and 28 of ASCE 7-22. The loads examined in this study are the base shear and the uplift for all buildings and end bay uplift and end bay horizontal thrust of low-rise-shaped ($h/w \le 1$) buildings. For each

Table 2. The Wang and Kopp (2020b) wind tunnel geometries

Building No.	Width, w (m)	Depth, d (m)	Height, h (m)	w/d	h/w
1	12	48	12	0.25	0.25
2	12	36	12	0.33	0.33
3	12	30	12	0.4	0.4
4	12	24	12	0.5	0.5
5	12	18	12	0.67	0.67
6	12	12	12	1.0	1.0
7	12	48	24	0.25	0.5
8	12	36	24	0.33	0.67
9	12	30	24	0.4	0.8
10	12	24	24	0.5	1.0
11	12	18	24	0.67	1.33
12	12	12	24	1.0	2.0
13	6	24	24	0.25	1.0
14	6	18	24	0.33	1.33
15	6	15	24	0.4	1.6
16	6	12	24	0.5	2.0
17	6	9	24	0.67	2.67
18	6	6	24	1.0	4.0
19	6	24	48	0.25	2.0
20	6	18	48	0.33	2.67
21	6	15	48	0.4	3.2
22	6	12	48	0.5	4.0
23	6	9	48	0.67	5.33
24	6	6	48	1.0	8.0

building model, the time series of the aerodynamic loads are integrated from the pressure data measured in wind tunnel tests.

A moving-average frequency filter is applied to each time series to approximate the mechanical admittance effects on the response to the turbulent gust loading (Guo et al. 2024, 2025). The current analysis applies moving-average filters to the pressure data with 1/3 s for $h/w \leq 2$ and 1 s for $h/w \geq 4$, based on discussion with the advisory group for this project (Guo et al. 2025). This concept requires some further explanation since it is both new and related to (1) the difference in philosophical approaches for the directional and envelope methods, as well as (2) the nature of the data and theory used in the development of these methods.

It worth emphasizing that the load coefficients given by the building codes are fundamentally based on the concept of ESWL. In other words, these are not raw area-averaged aerodynamic coefficients. Chapters 27 and 28 of ASCE 7 address this concept through distinct frameworks. In Chapter 27, the theoretical solution of Solari (1993a, b) is adopted, in which the resonant component of the structural response is derived by integrating the mechanical admittance function (MAF) over a narrow band around the fundamental frequency, and combined with a background component, which is derived via the aerodynamic admittance functions (AAF) and quasi-steady theory. Chapter 28, in contrast, adopts an empirical approach by using directly measured peak loads from wind tunnel experiments, under assumption that the building structure is perfectly rigid with the MAF of unity across all frequencies. In the proposed unified method, these approaches are synthesized: the measured peaks are used to obtain the background component of the pressure coefficient. This captures the effects of the body-generated turbulence, while allowing the theoretical framework for the resonant component to be retained. With this formulation, one remaining issue is that the effects of mechanical admittance functions at higher frequencies are not considered. Since the MAFs typically exhibit decaying values at higher frequency, neglecting it leads to overestimation of the fluctuating and peak reactions, impacting the statistics significantly. In the theoretical solution of Chapter 27, this issue is not addressed directly, but is accounted for by attenuation of the high-frequency energy, resulting from the filters applied to the velocity spectra and the decaying vale of the aerodynamic admittance functions at the higher frequencies. In Chapter 28, this issue is ignored under the perfectly rigid assumption. However, such an assumption is not realistic even for low-rise structures, for which the dynamic effects may also be significant (see Wang et al. 2024). Thus, the use of the temporal filter in the current work represents a compromise between the two methods, which we interpret as representing the mechanical admittance effects.

The peak aerodynamic load coefficients, $\widehat{Cp}$, corresponding to a 57% probability of nonexceedance in 1 h (3,600 s) full-scale, are then obtained using the Lieblein BLUE method (Lieblein 1974). The peak loads in pressure coefficient form are converted to $[GCp]$ considering the 3-s gust speed,

$$[GCp] = \frac{\widehat{Cp}}{(1 + g_u I_u)^2} \tag{14}$$

where g_u and I_u = peak factor and turbulence intensity of the reference velocity, respectively. Further details of the calculation can be found in Guo et al. (2024) and Acosta et al. (2024).

To examine the differences arising in the peak coefficients, the mean pressure coefficients in the current data set are first examined

Table 3. The Ho et al. (2005) wind tunnel building geometries

Building No.	Roof slope (tangent)	Width, w (m)	Depth, d (m)	Eave height, h_e (m)	Building No.	Roof slope (tangent)	Width, w (m)	Depth, d (m)	Eave height, h_e (m)
1	12/12	24.38	38.1	12.19	14	12/12	48.77	76.2	12.19
2				9.75	15				7.32
3				7.32	16				5.49
4				4.88	17				3.66
5	0.25/12	24.38	38.1	12.19	18	12/12	36.58	57.15	12.19
6				9.75	19				7.32
7				7.32	20				5.49
8				5.49	21				4.88
9				3.66	22				3.66
10	12/12	12.19	19.05	12.19	23	0.5/12	15.24	30.48	4.88
11				7.32	24				3.66
12				5.49	25	0.5/12	15.24	53.34	4.88
13				3.66	26				3.66

and compared to those in ASCE 7-22 Fig. 27.3-1. Second, to examine the differences between the measured and theoretical values of G, the following are investigated: (1) aerodynamic admittance functions, to understand how these affect the background response factor, Q, (2) the effect of filtering on the peaks, and (3) the statistical distributions, to understand how these affect the peak factors.

The peak factor, g, the gust effect factor, G, as well as the skewness and kurtosis, are used to study the statistical distributions of the aerodynamic loads. The first two parameters are calculated from

$$g = \frac{\widehat{Cp} - \overline{Cp}}{\sigma_{Cp}} \tag{15}$$

$$G = \frac{\widehat{Cp}}{\overline{Cp}} \tag{16}$$

where $\overline{Cp}$ and σ_{Cp} = mean and standard deviation of the load coefficient time series, respectively.

Results and Discussion

Examination of Role of Building Shape and Nondimensional Geometric Parameters

Fig. 27 3-1 of ASCE 7-22 provides the basic pressure coefficients for buildings of all heights with the directional method. As noted previously, in this figure, the windward wall and side wall both have constant pressure coefficients (although they have different reference dynamic pressures). In other words, these building surfaces are assumed not to have a dependence on the building geometry. However, the leeward wall has a dependence on L/B while the roof depends on h/L and the roof slope, θ. While the leeward wall has a uniform pressure distribution, the roof has zones, the size of which depend on h/L.

Fig. 28 3-1 of ASCE 7-22 provides the pressure coefficients for low-rise buildings with the envelope method. These pressure distributions are more complex, with distinct pressure zones on all surfaces. However, aside from some functional dependence on the zone sizes and roof slope, the pressure coefficients do not depend on the basic building dimensions: h, w, and d. Thus, an inherent assumption is that all low-rise buildings (with a fixed roof slope) have the same wind load coefficients and that the design loads only vary with the dynamic wind pressure, i.e., the basic wind speed, building height, and the terrain category. This contrasts with the directional method, where the along-wind base shears (and overturning moments) and roof uplift both depend on the building shape and size.

Wang and Kopp (2020a, b) examining the same two data sets as the current paper determined the geometric parameters that control the wind loads for each building surface. Table 4 summarizes their findings, providing the primary controlling factor for the building surface loads. For example, windward walls are controlled by the wall aspect ratio, h/B, for buildings with $h/w \leq 4$, while for buildings with $h/w > 4$, the load coefficient is basically constant.

Fig. 2 depicts the variations of uplift, wall-averaged pressure coefficients, and base shear for low-rise buildings ($h/w < 1$) with low-sloped roofs, based on the parameters determined by Wang and Kopp (2020a). Fig. 3 shows the same for mid- and high-rise buildings ($h/w \geq 1$), based on Wang and Kopp (2020b). Gust pressure coefficients, $[GCp]$, from the experimental data can be compared with the values arising from ASCE-22 Chapters 27 and 28, which are discussed as follows.

Table 4. Geometric parameters that control the wind loads for building surfaces

Building types	Critical parameter: Roofs, leeward and sidewalls	Critical parameter: Windward walls
Low-rise ($h/w \leq 1$)	h/L	h/B
Mid-rise	L/B and h/w	h/B
High-rise ($h/w \geq 4$)	L/B	$h/B > 4 \sim$ constant

Sources: Data from Wang and Kopp (2020a, b).

Chapter 28 Pressure Distributions

As discussed above, the Chapter 28 pressure coefficients are not a function of the basic geometric parameters of the buildings, h, d, and w. However, Fig. 2 provides the experimental results indicating the strong dependence on these parameters for low-rise building wind loads. The results using Fig. 28.3-1 of ASCE 7-22 are included, which are approximately constant and fail to capture the trends of the experimental data.

Considering Load Case 1 in Fig. 28.3-1, there are four pressure zones on a building roof. These zones do not capture the variation of pressure for low-slope roofs, which have maximum suctions near windward edges with decreasing magnitude as a function of distance from the edge, as depicted by Wang and Kopp (2020a). For Load Case 2, there are two pressure zones near the gable end; however, these zone sizes (controlled by the parameter, a, defined as the smallest between the 10% of building least horizontal dimension and 40% of the building height) do not vary in the way that the actual aerodynamics show. Morrison and Kopp (2018) provide a detailed examination of the variation of pressure zones for component and cladding loads, which indicate that it should be a function of building height, and also should apply to the variation of MWFRS loads. As a result, the roof uplift estimated by Chapter 28 is conservative for $h/L < \sim 0.5$, while it is unconservative (low) for $h/L > \sim 0.5$. For base shear, the Chapter 28 results are adequate for $h/B < \sim 0.2$ but are unconservative (low) for $h/B > \sim 0.2$. In fact, the base shears in Chapter 28 are only about 65% of the measured values for $h/B > \sim 0.5$.

St. Pierre et al. (2005) also examined the NIST aerodynamic database (Ho et al. 2005), using the same influence function approach as Stathopoulos (1979). While these authors used slightly different statistical analyses of peak loads (i.e., probability levels and filtering), their results show similar trends indicating issues with the pressure distributions in the existing provisions. Readers are referred to this work to see detailed comparisons for bay and frame loads.

Chapter 27 Pressure Distributions

As discussed above, Chapter 27 has some pressure coefficients with dependence on nondimensional building parameters, while others do not. Figs. 2 and 3 compare these with the experimental data using a gust effect factor for rigid buildings, $G = 0.85$.

For roof uplift, Fig. 2(a) indicates that Chapter 27 captures the variation of the loads accurately with the linear dependence on h/L for low-rise buildings. The distribution of pressures is not exact though, since the magnitude of the slope of the $(G)(Cp)$ versus h/L curve is slightly unconservative. Fig. 3(a) indicates that the trends are also reasonable for mid- and high-rise buildings, although not as good for low-rise buildings. This is not surprising since the best parameter to capture the trend of the uplift for mid- and high-rise buildings is L/B (Wang and Kopp 2020a, b), while the parameter used in Chapter 27 is still h/L. The uplift tends to be underestimated for approximately $0.3 < L/B < 1$.

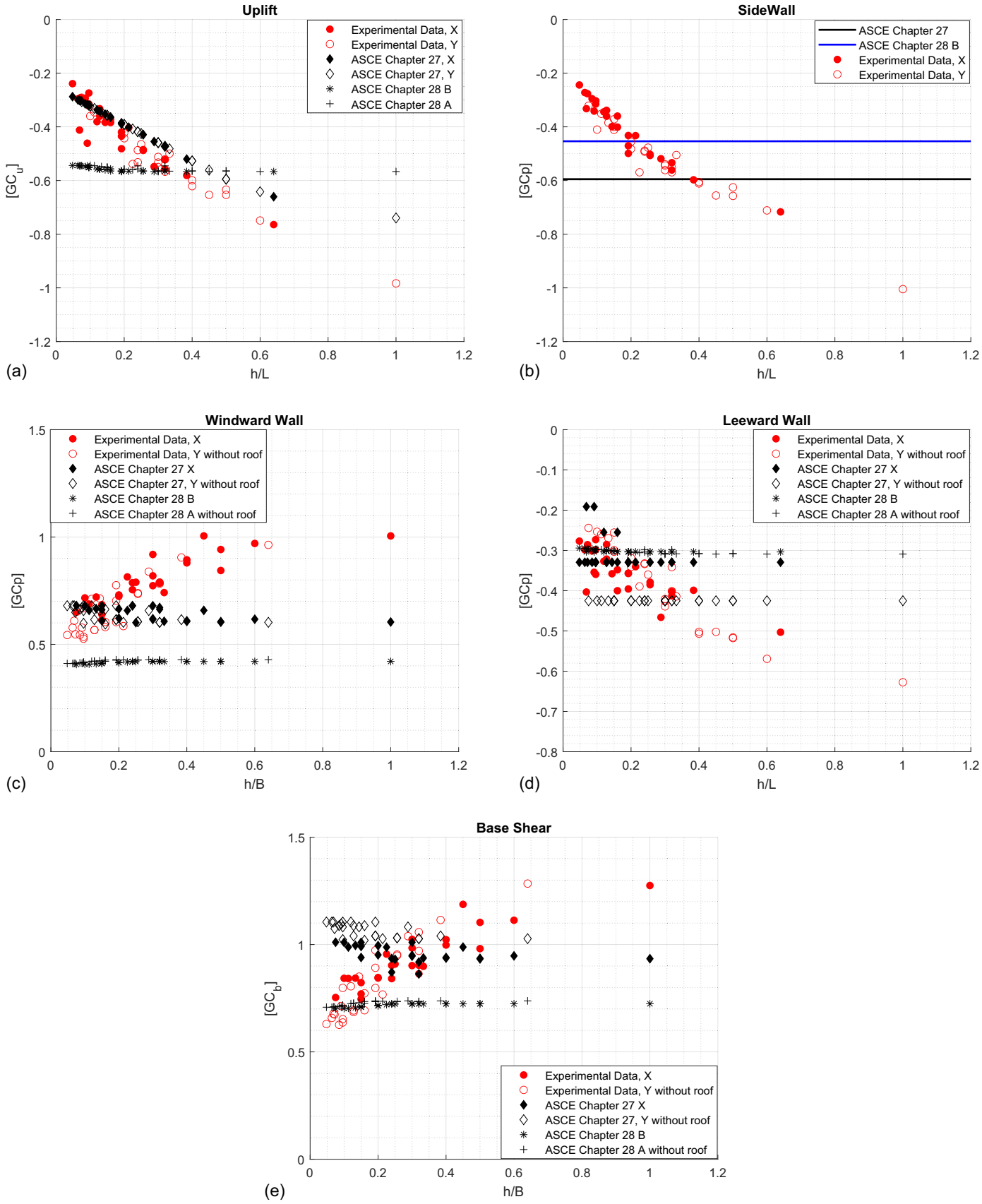

Fig. 2. Plots of peak load and area-averaged pressure coefficients as a function of nondimensional parameters for low-rise buildings with low-slope roofs: (a) roof uplift coefficient, $[GC_u]$, as function of h/L; (b) area-averaged side wall pressure coefficient as function of h/L; (c) area-averaged windward wall pressure coefficient as a function of h/B; (d) area-averaged leeward wall pressure coefficient as a function of h/L; and (e) base shear coefficient, $[GC_b]$, as function of h/B.

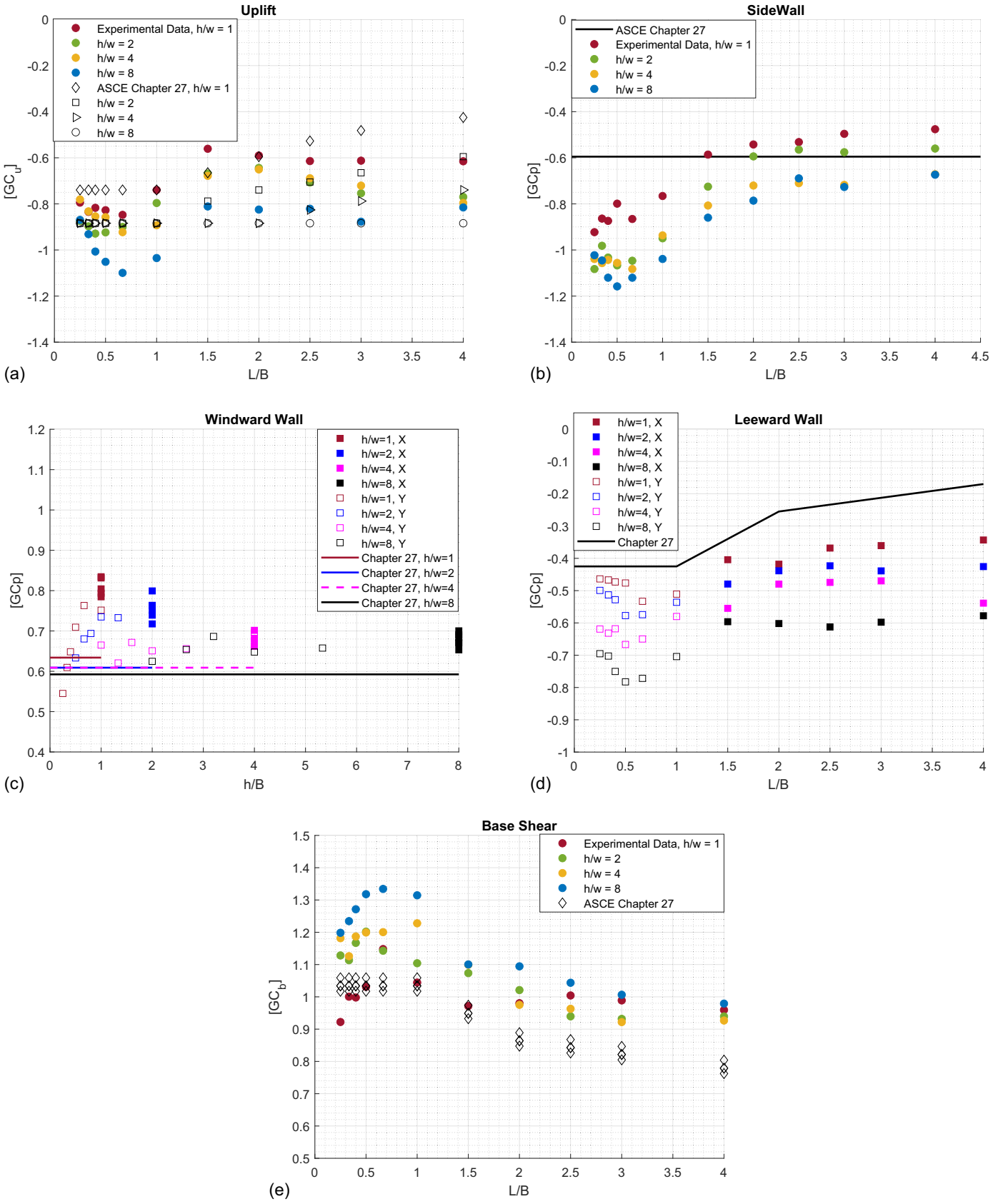

Fig. 3. Plots of peak load and area-averaged pressures coefficients as a function of nondimensional parameters for mid and high-rise buildings with flat roofs: (a) roof uplift coefficient, $[GC_u]$, as function of L/B; (b) area-averaged side wall pressure coefficient as function of L/B; (c) area-averaged windward wall pressure coefficient as a function of H/B; (d) area-averaged leeward wall pressure coefficient as a function of L/B; and (e) base shear coefficient, $[GC_b]$, as function of L/B.

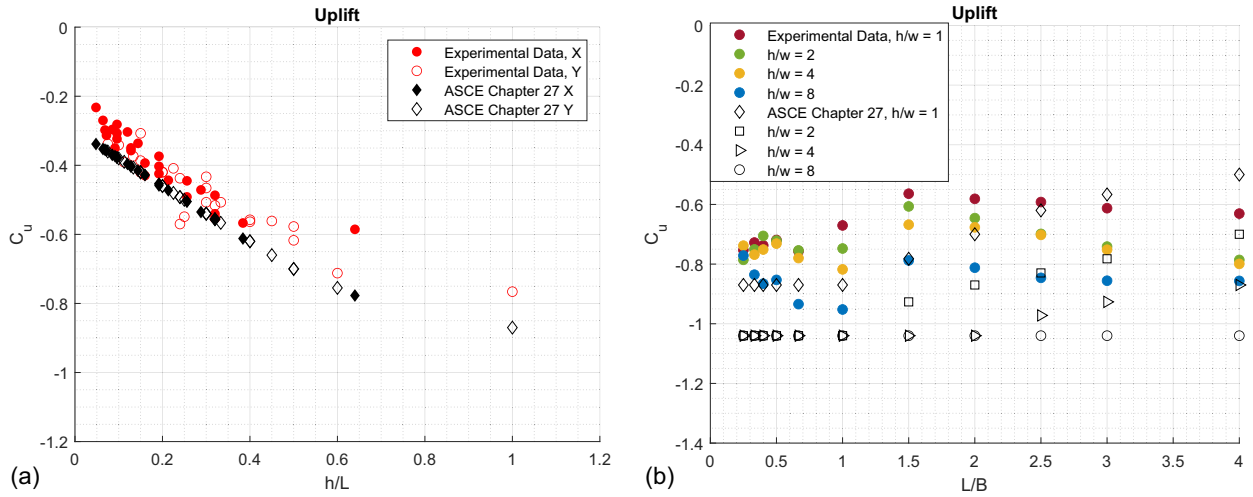

Fig. 4. Mean uplift coefficients, C_u, as a function of (a) h/L for low-rise buildings; and (b) L/B for mid-rise and high-rise buildings.

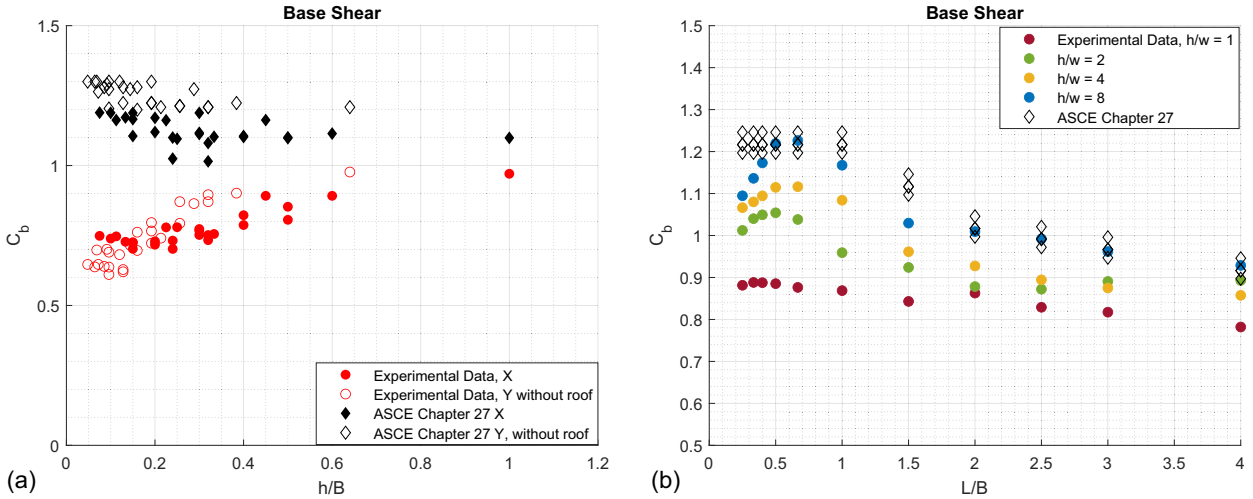

Fig. 5. Mean base shear coefficients, C_b, as a function of (a) h/B for low-rise buildings; and (b) L/B for midrise and high-rise buildings.

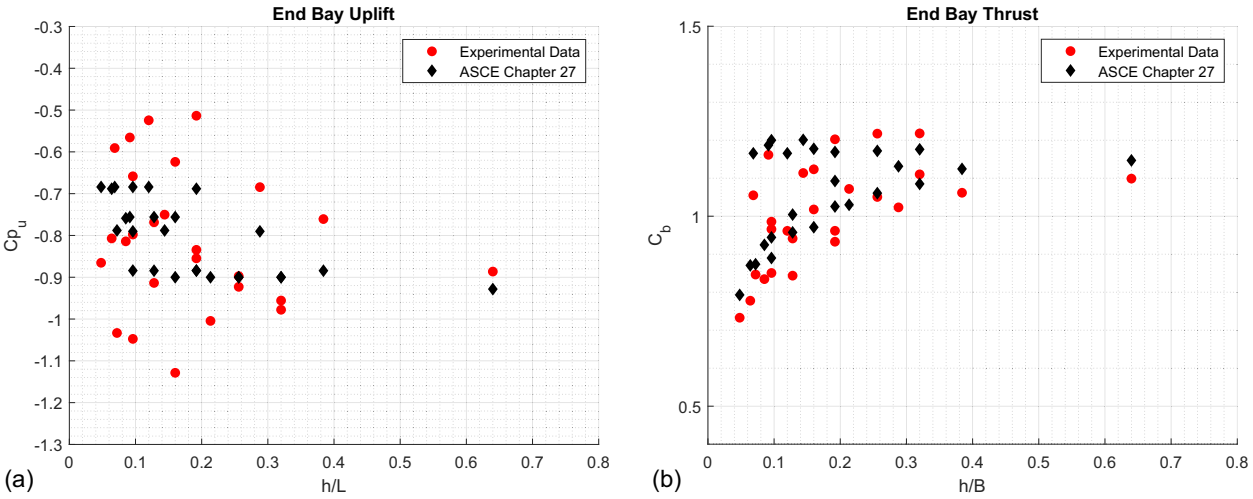

Fig. 6. Mean (a) end bay uplift coefficients, C_u, as a function of h/L; and (b) end bay horizontal thrust, C_b, as a function of h/B for low-rise buildings.

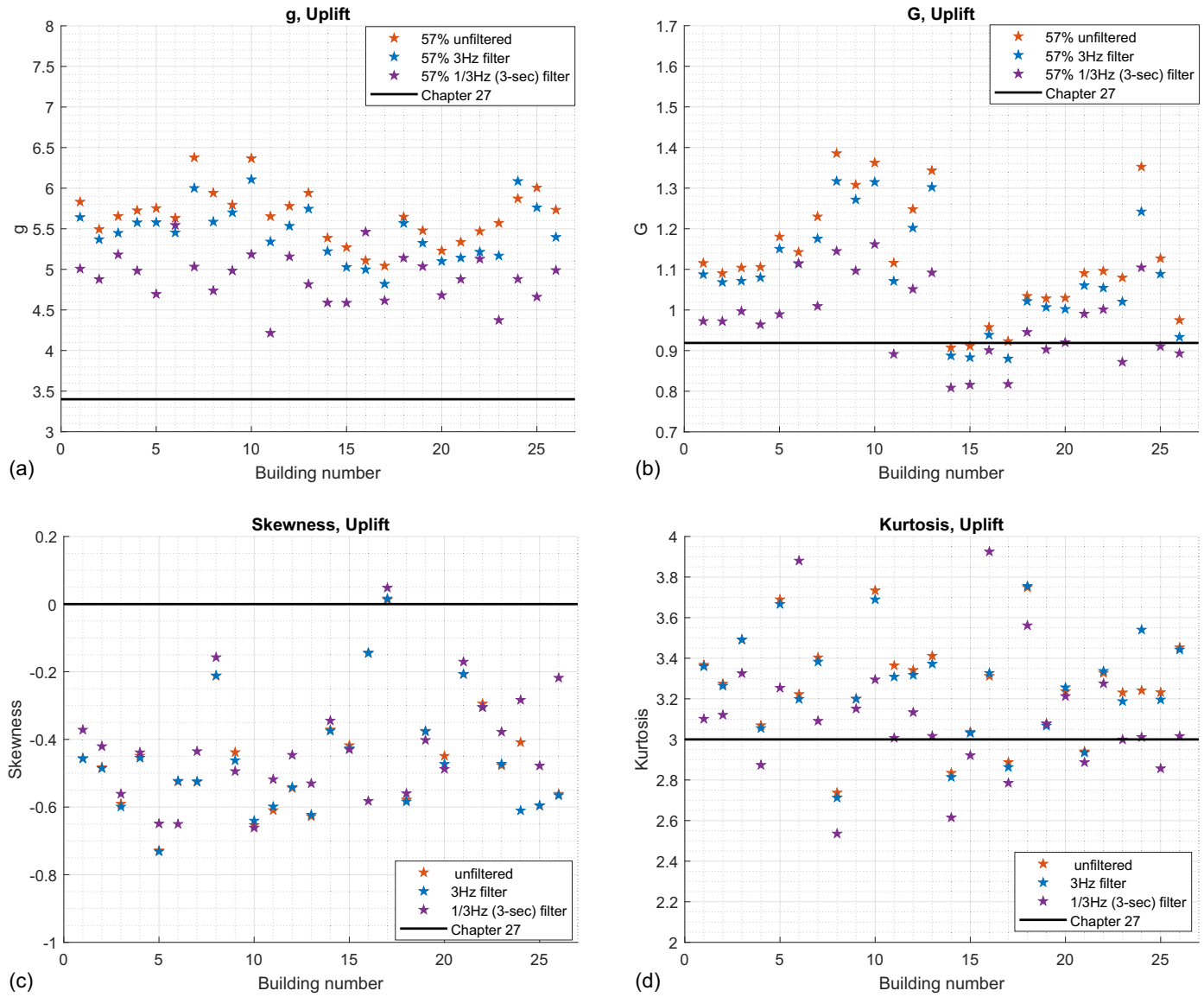

Fig. 7. (a) Peak factors; (b) gust effect factors; (c) skewness; and (d) kurtosis of roof uplift for low-rise buildings (NIST database) in open terrain for the critical wind direction. The building geometries for the building numbers are provided in Table 3.

For sidewalls, which have a constant value, the Chapter 27 provisions do not follow the trends at all, as shown in Figs. 2(b) and 3(b). As discussed above, the sidewalls tend to be like the roof, having large regions of separated flow near leading edges. As a result, the sidewall pressures for many buildings will be too low, especially for larger values of $h/L > \sim 0.5$ and $B/L > \sim 0.5$.

For the windward wall pressures, the experimental data appear to be strongly dependent on h/B for low-rise buildings [Fig. 3(c)], as discussed in the section "Results and Discussion." This dependence is less significant for mid- and high-rise buildings, while some variation can be observed versus h/w [Fig. 3(c)]. The Chapter 27 results are, however, nearly constant, with only some slight variation due to q_z, and does not follow the trends of the experimental data.

For the leeward wall pressures, the results provided by Chapter 27 are based on L/B, which captures the trend reasonably well for the mid- and high-rise buildings, although it misses the variation due to h/w and underestimates the magnitude of the pressure coefficients [Fig. 3(d)]. For the low-rise buildings, the experimental data have dependence on the ratio of h/L, which the Chapter 27 results fail to match.

For base shears, which are the instantaneous combination of the windward and leeward walls, the dependence on building geometry is complicated since the windward and leeward walls are controlled by different parameters. For low-rise buildings, the Chapter 27 provisions do not follow the trends, although they tend to conservatively (safely) envelope the experimental data, as can be seen in Fig. 2(e). For mid- and high-rise buildings, as shown in Fig. 3(e), the Chapter 27 trend is correct although the base shears are underestimated by up to 30%. This appears to be due to both windward and leeward wall pressures being larger in the experimental data. Since the trends are correct in Chapter 27, there are issues with the magnitude that need to be examined, which is undertaken as follows.

Comparison of Measured and Theoretical Gust Effect Factors

Mean Aerodynamic Loads

Figs. 4 and 5 depict the mean uplift and base shear coefficients, respectively. For the roof uplift, the data in Fig. 4 indicate that

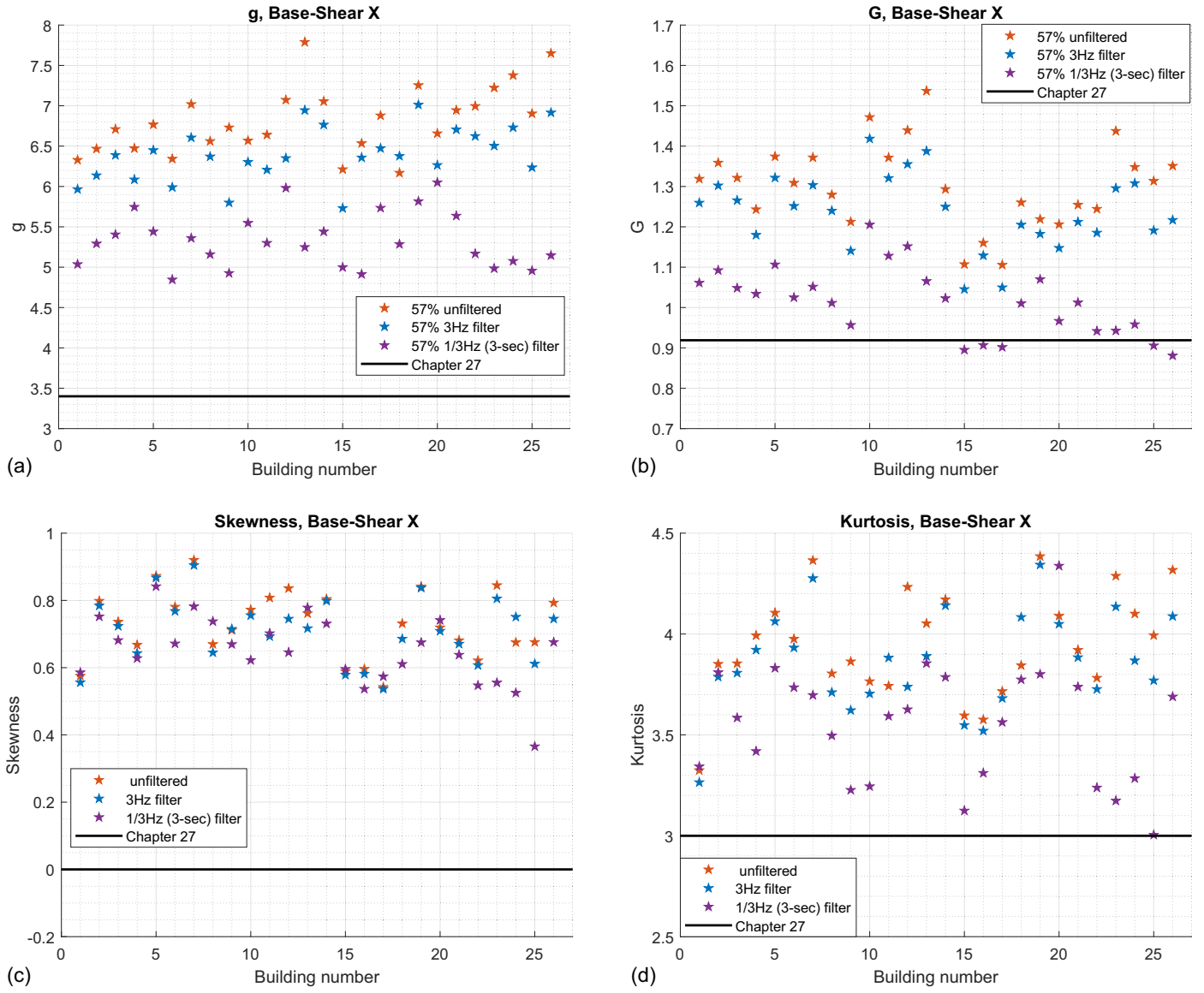

Fig. 8. (a) Peak factors; (b) gust effect factors; (c) skewness; and (d) kurtosis of base shear in x-direction (parallel to ridge) for low-rise buildings (NIST database) in open terrain for the critical wind direction. The building geometries for the building numbers are provided in Table 3.

the mean values in ASCE 7 adequately match the patterns of the experimental data, with the ASCE 7 provisions having slightly larger magnitudes. In contrast, the ASCE 7 mean base shear coefficients are quite conservative (i.e., larger by about 100%) and do not follow the pattern with h/B for low-rise buildings [Fig. 5(a)]. Fig. 6 depicts the end bay uplift and end bay horizontal thrust for low-rise buildings. These mean loads are well captured by the existing Chapter 27 provisions. Thus, the overall pressure distribution is not particularly good since it significantly over-estimates the overall mean loads but with reasonably accurate end bay/frame loads. For midrise and high-rise buildings, the values of the mean base shear are also larger than the experimental data (except for $h/w = 8$, for which the match is excellent). However, ASCE 7 generally has the same load pattern, as shown in Fig. 5(b).

In summary, it is observed that mean load coefficients are adequately modeled except for low-rise buildings where the overall mean base shears tend to be over-estimated. Since the Chapter 27 provisions under-estimate the experimental loads for a range of building geometries, although not all of them, these differences are attributed to gust (turbulence) effects that lead to gust effect factors larger than the standard. We examine this in the next section.

Statistical Distributions, Peak Factors, and Effects of Filtering

Figs. 7–9 provide details for on the statistical distributions for roof uplift and base shear for low-rise buildings and for overturning moments for midrise and high-rise buildings. For the low-rise buildings, the peak factors [Figs. 7(a) and 8(a)] indicate values significantly larger than the Gaussian values used for the development of ASCE 7, i.e., $g_P = 3.4$. While temporal filtering significantly reduces the peak factors, for the low-rise buildings, the reduction typically changes the peak factor from between 5–7 to between 4.5–5.5 for the $1/3$ s (3 Hz) filter. Figs. 7(c and d) and 8(c and d) of the skewness and kurtosis, respectively, indicate significant non-Gaussian distributions for these low-rise buildings. Focusing on the $1/3$ s (3 Hz) filter results, the gust effect factors for the uplift and base shear are in the range of 1.1 to 1.3, significantly above the theoretical values. In contrast, for the 3 s ($1/3$ Hz) filter (used in

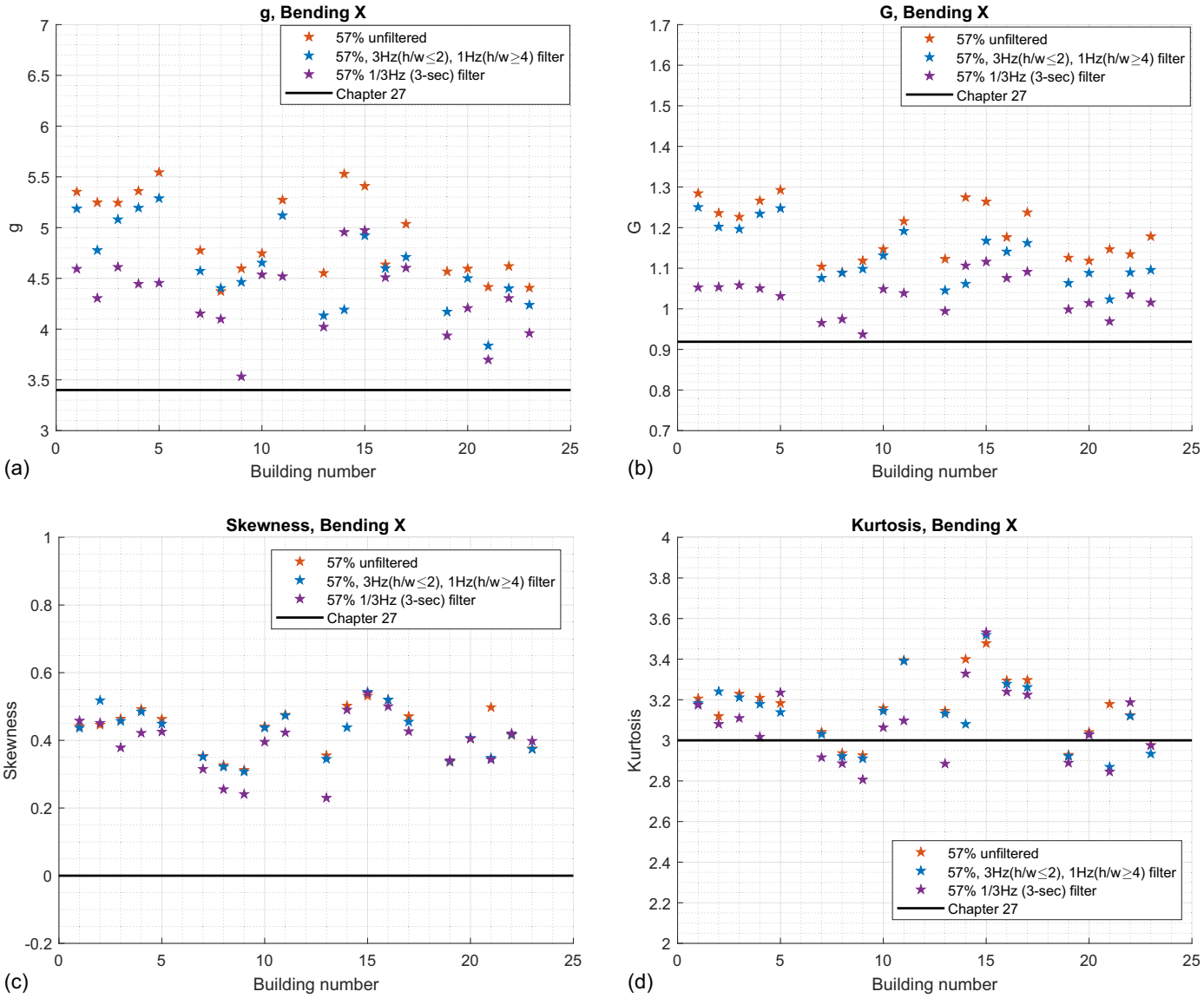

Fig. 9. (a) Peak factors; (b) gust effect factors; (c) skewness; and (d) kurtosis of overturning moments in x-direction midrise and high-rise buildings in open terrain for the critical wind direction. The building geometries for the building numbers are provided in Table 2.

the development of the current ASCE values) have G in the range of 1.0–1.1, also greater than the theoretical value of 0.925. Building size effects can be observed for the gust effect factors. For example, for the uplift coefficient, the values of G with 1/3 s (3 Hz) filter generally range between 1.1 and 1.3 for buildings with plan dimensions of 12.19 m × 19.05 m [building number 10–13 in Fig. 7(b)], while for plan dimensions of 48.77 × 76.2 m (building number 14–17), these values drop to around 0.9. In general, the ASCE 7 underestimation of the gust effect is most significant for smaller building models and less obvious for larger ones.

For the taller buildings, it is evident that high-rise building loads are less skewed, leading to lower peak factors. However, the values are such that they are still higher than those used in the development of the ASCE 7 provisions. The gust effect factor is lower with larger h/w values, dropping from about 1.2 for $h/w = 1$ to 1.0–1.1 for $h/w = 8$ for the 1 s (1 Hz) filter, and about 1.0 for the 3 s (1/3 Hz) filter. Thus, all observed gust effect factors are larger than the theoretical ASCE 7 values. This can be attributed to non-Gaussian behavior in the wind loads combined with the effect of temporal filters.

Aerodynamic Admittance Functions

Representative aerodynamic admittance functions are depicted in Figs. 10 and 11. For high-rise buildings, $h/w \geq 4$, Solari and Kareem (1998) admittance function is a good representation of the experimental data. However, for the low- and midrise data it underestimates the results for $h/w \leq 2$ for reduced frequencies, $f\sqrt{BH}/\overline{u}_{0.5H}$, above 0.1. A portion of this effect is likely due to the filtering, although for regions of separated flow, the active turbulence region is above reduced frequencies of 0.1 (Morrison and Kopp 2018). So, while the admittance does not play a role in altering the gust effect factors for high-rise buildings, it is of importance for low- and midrise buildings.

Conclusions

In this paper, the differences in aerodynamic loading between the existing provisions for MWFRS in ASCE 7 and a set of 50 buildings in wind tunnel databases are examined. The conclusions are summarized as follows.

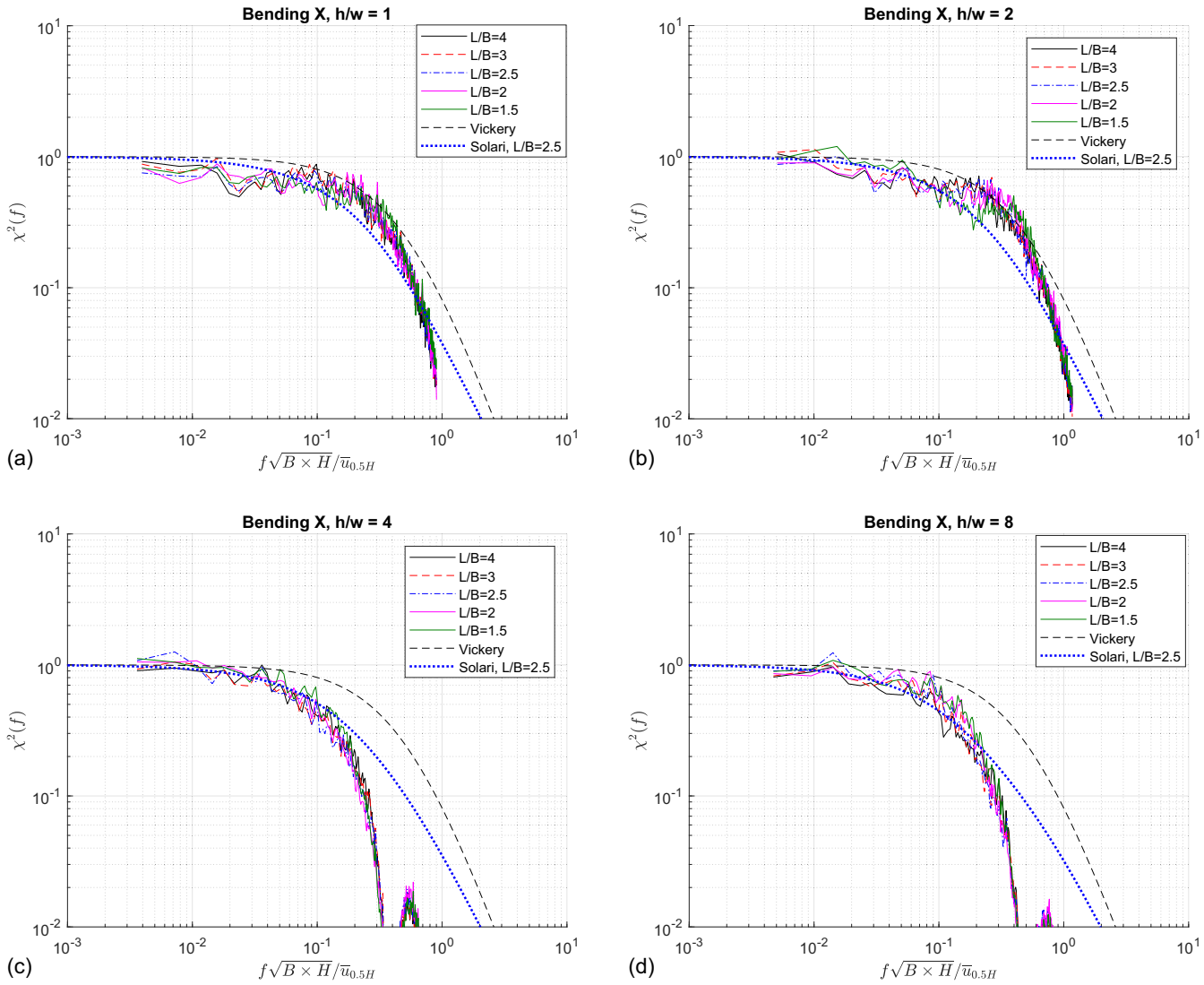

Fig. 10. Aerodynamic admittance functions for filtered overturning moments for a wind direction of 90° in open terrain for midrise and high-rise buildings for (a) $h/w = 1$; (b) $h/w = 2$; (c) $h/w = 4$; and (d) $h/w = 8$.

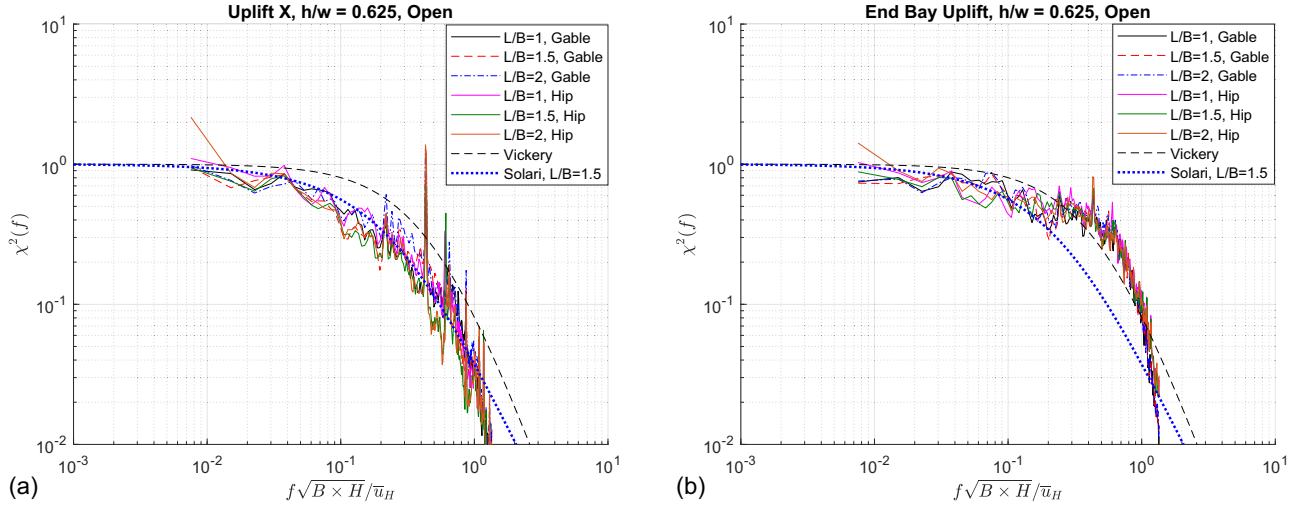

Fig. 11. Aerodynamic admittance functions for filtered (a) uplift; and (b) end-bay uplift for a wind direction of 90° in open terrain for 6/12-sloped roof, low-rise buildings with $h/w = 0.625$.

The use of nondimensional building shape parameters allows for more accurate modeling of the wind loads. This has some effects on Chapter 27 loads but is particularly important for Chapter 28 where differing building shapes are not accounted for. In the original 1970s studies that led to the envelope method, the data sets had h/w ratios only in the range of 0.2 to 0.4. This has a significant effect on base shears and roof uplift for buildings since wall aspect ratios, h/B and h/L, have a significant effect on these loads. Chapter 28 also has size-of-building issues since the pressure zones do not scale with the size of the building in the way that the aerodynamics actually behave. This leads to loads on parts of buildings, like frames and bays, which are unconservative, as previously shown by St. Pierre et al. (2005).

The experimental data also have some significantly different load magnitudes from those of Chapter 27 that cannot be accounted for by building geometry parameters alone. Chapter 27 is based on using mean wall-averaged pressure coefficients together with a calculated (theoretical) gust effect factor. Assessment of the mean coefficients indicates that they are mostly reasonable, although for certain building configurations they can be rather conservative (i.e., safe).

The primary issue with the Chapter 27 provisions is that the theoretically-calculated gust effects do not capture the measured turbulence effects. Detailed analysis indicates that the use of quasi-steady theory is mostly reasonable such that the calculated background response factor, Q, is reasonable. The primary issue with the theoretical model is that the pressure and load variations are non-Gaussian, which leads to peak factors and gust effect factors that are substantially higher than the theoretical values that were used in the development of the standard (i.e., $g = 3.4$; $G = 0.92$), even before the gust effect factor was reduced further to $G = 0.85$. It is observed that this non-Gaussianity is connected to the building geometry and is, therefore, connected to the flow patterns and building-generated vortex structures around all building surfaces. The arbitrary use of a 3-s moving average filter of the background response has a large effect on non-Gaussian peak values used in ASCE 7. All these features lead to gust effect factors that should be much larger than the assumed value of $G = 0.85$ in ASCE 7.

Data Availability Statement

Some or all data, models, or code that support the findings of this study are available from the corresponding author upon reasonable request.

Acknowledgments

This work was funded by the Structural Engineering Institute of the ASCE. The authors gratefully acknowledge the support of an Advisory Group made up of members of the ASCE 7 Wind Loads Sub-Committee, in particular Don Scott who chaired the Advisory Group, and Larry Griffis, Tim Reinhold, and Peter Vickery who provided significant guidance.

Author Contributions

Gregory A. Kopp: Conceptualization; Formal analysis; Funding acquisition; Investigation; Methodology; Project administration; Supervision; Writing – original draft; Writing – review and editing. Jin Wang: Formal analysis; Investigation; Methodology; Writing – review and editing. Yitian Guo: Data curation; Formal analysis; Investigation; Methodology; Writing – review and editing. Stefano Brusco: Formal analysis; Investigation; Writing – review and editing. Timothy John Acosta: Data curation; Formal analysis; Investigation; Writing – review and editing.

References

Acosta, T. J., S. Brusco, Y. Guo, J. Wang, and G. A. Kopp. 2024. *Consolidation of the ASCE 7 MWFRS provisions: Part 2. Wind tunnel experiments on buildings with 6:12 roof slopes*. London: Western Univ.

Akins, R. E., J. A. Peterka, and J. E. Cermak. 1977. "Mean force and moment coefficients for buildings in turbulent boundary layers." *J. Wind Eng. Ind. Aerodyn.* 2 (3): 195–209. https://doi.org/10.1016/0167-6105(77)90022-8.

Davenport, A. G. 1967. "Gust loading factors." *J. Struct. Div.* 93 (3): 11–34. https://doi.org/10.1061/JSDEAG.0001692.

Guo, Y., G. A. Kopp, J. Wang, T. J. Acosta, and S. Brusco. 2024. *Consolidation of the ASCE 7 MWFRS provisions: Part 1. Methodology for obtaining the new aerodynamic coefficients and load cases*. London: Western Univ.

Guo, Y., J. Wang, T. J. Acosta, S. Brusco, and G. A. Kopp. 2025. "Methodology for obtaining aerodynamic coefficients for unified wind loading provisions in ASCE 7." *J. Struct. Eng.* 151 (11): 04025182. https://doi.org/10.1061/JSENDH.STENG-14983.

Ho, T. E., D. Surry, D. Morrish, and G. A. Kopp. 2005. "The UWO contribution to the NIST aerodynamic database for wind loads on low buildings: Part 1. Archiving format and basic aerodynamic data." *J. Wind Eng. Ind. Aerodyn.* 93 (1): 1–30. https://doi.org/10.1016/j.jweia.2004.07.006.

Holmes, J. D., A. C. Allsop, and J. D. Ginger. 2014. "Gust durations, gust factors and gust response factors in wind codes and standards." *Wind Struct.* 19 (3): 339–352. https://doi.org/10.12989/was.2014.19.3.339.

Lieblein, J. 1974. *Note on simplified estimators for Type I extreme-value distribution*. Rep. No. 75, 637. Gaithersburg, MD: NIST.

Morrison, M. J., and G. A. Kopp. 2018. "Effects of turbulence intensity and scale on surface pressure fluctuations on the roof of a low-rise building in the atmospheric boundary layer." *J. Wind Eng. Ind. Aerodyn.* 183 (Dec): 140–151. https://doi.org/10.1016/j.jweia.2018.10.017.

Solari, G. 1993a. "Gust buffeting. I: Peak wind velocity and equivalent pressure." *J. Struct. Eng.* 119 (2): 365–382. https://doi.org/10.1061/(ASCE)0733-9445(1993)119:2(365).

Solari, G. 1993b. "Gust buffeting. II: Dynamic alongwind response." *J. Struct. Eng.* 119 (2): 383–398. https://doi.org/10.1061/(ASCE)0733-9445(1993)119:2(383).

Solari, G., and A. Kareem. 1998. "On the formulation of ASCE7-95 gust effect factor." *J. Wind Eng. Ind. Aerodyn.* 77 (Sep): 673–684. https://doi.org/10.1016/S0167-6105(98)00182-2.

Stathopoulos, T. G. 1979. "Turbulent wind action on low rise buildings." Ph.D. thesis, Faculty of Graduate Studies, Univ. of Western Ontario.

St. Pierre, L. M. S., G. A. Kopp, D. Surry, and T. C. E. Ho. 2005. "The UWO contribution to the NIST aerodynamic database for wind loads on low buildings: Part 2. Comparison of data with wind load provisions." *J. Wind Eng. Ind. Aerodyn.* 93 (1): 31–59. https://doi.org/10.1016/j.jweia.2004.07.007.

Wang, J., and G. A. Kopp. 2020a. "Comparisons of aerodynamic data with the main wind force–resisting system provisions of ASCE 7-16. I: Low-rise buildings." *J. Struct. Eng.* 147 (3): 04020347. https://doi.org/10.1061/(ASCE)ST.1943-541X.0002925.

Wang, J., and G. A. Kopp. 2020b. "Comparisons of aerodynamic data with the main wind force–resisting system provisions of ASCE 7-16. II: Mid-and high-rise buildings." *J. Struct. Eng.* 147 (3): 04020348. https://doi.org/10.1061/(ASCE)ST.1943-541X.0002922.

Wang, J., G. A. Kopp, and C. Yang. 2024. *Flexibility study of moment-framed low-rise metal buildings*. London: Western Univ.